2015

Integrated visible and near-infrared, shortwave infrared, and longwave infrared full-range hyperspectral data analysis for geologic mapping

Kruse, Fred A.

F. Kruse, "Integrated visible and near-infrared, shortwave infrared, and longwave infrared full-range hyperspectral data analysis for geologic mapping," Journal of Applied Remote Sensing, Vol. 9, 2015, 20 p.
https://hdl.handle.net/10945/46692

Journal of
Applied Remote Sensing

RemoteSensing.SPIEDigitalLibrary.org

Integrated visible and near-infrared, shortwave infrared, and longwave infrared full-range hyperspectral data analysis for geologic mapping

Fred A. Kruse

SPIE.

Integrated visible and near-infrared, shortwave infrared, and longwave infrared full-range hyperspectral data analysis for geologic mapping

Fred A. Kruse*
Naval Postgraduate School, Physics Department and Remote Sensing Center, 833 Dyer Road, Monterey, California 93943, United States

Abstract. Airborne visible/infrared imaging spectrometer (AVIRIS) and spatially coincident hyperspectral thermal emission spectrometer (HyTES) data were used to map geology and alteration for a site in northern Death Valley, California and Nevada. AVIRIS with 224 bands from 0.4 to 2.5 μm were converted to reflectance. HyTES data with 256 bands covering 8 to 12 μm were converted to emissivity. Two approaches were investigated for integration of the datasets for full spectrum analysis. A combined (integrated) bands method utilized 332 spectral bands spanning both datasets. Spectral endmembers were extracted, and the predominant material at each pixel was mapped for the full spectral range using partial unmixing. This approach separated a variety of materials, but it was difficult to directly relate mapping results to surface properties. The second method used visible to near-infrared, shortwave infrared, and longwave infrared data independently to determine and map key endmembers in each spectral range. AVIRIS directly mapped a variety of specific minerals, while HyTES separated and mapped several igneous rock phases. Individual mapping results were then combined using geologically directed logical operators. The full-range results illustrate that integrated analysis provides advantages over use of just one spectral range, leading to improved understanding of the distribution of geologic units and alteration. [DOI: 10.1117/1.JRS.9.096005]

Keywords: hyperspectral data fusion; hyperspectral imaging; spectral geology; visible near-infrared; shortwave infrared; longwave infrared; multimodal spectral mapping; northern Death Valley remote sensing.

Paper 15411P received Jun. 3, 2015; accepted for publication Aug. 17, 2015; published online Sep. 23, 2015.

1 Introduction

Identification of minerals and other geologic materials using visible to near-infrared (VNIR), shortwave infrared (SWIR), and longwave infrared (LWIR) spectroscopy is well established.[1–12] This forms the basis for remote measurements using imaging spectrometry [also called hyperspectral imagery (HSI)], consisting of imagery in up to hundreds of contiguous spectral bands, with a spectrum at each image pixel.[13] Hyperspectral data in the VNIR-SWIR have been available for over 30 years, and analysis of these for geologic applications is considered mature.[14] LWIR multispectral data have also been available for a long time[15–17] and are often used in conjunction with VNIR-SWIR data.[18–20] LWIR HSI data, however, have been more difficult to obtain, are only slowly becoming more broadly available, and provide new capabilities that are just coming into routine use.[21,22] While typically analyzed in their separate wavelength ranges, there are some examples of using these individual HSI data modes together.[23–25] Fully integrated analysis is, however, still being explored. The research summarized here is part of ongoing full-range HSI data analysis efforts at the Naval Postgraduate School.[26–29]

*Address all correspondence to: Fred A. Kruse, E-mail: fakruse@nps.edu

1931-3195/2015/$25.00

1.1 *Objectives*

The objective of this research was to improve accurate identification and mapping of geologic materials utilizing the complementary information available from the full spectral range (0.4 to 12 μm). Airborne visible/infrared imaging spectrometer (AVIRIS) data spanning the VNIR-SWIR and spatially coincident hyperspectral thermal emission spectrometer (HyTES) data covering the LWIR spectral region were first analyzed utilizing a combined (integrated) bands full-range HSI analysis approach. These results were subsequently compared to information from individual wavelength range (modal) analyses combined using logical operators to determine and map key integrated endmembers. Results illustrate the complementary nature of the different spectral regions, provide insight into the strengths and pitfalls of joint versus modal analyses, and demonstrate improved hyperspectral mapping capabilities using the combined data.

1.2 *Northern Death Valley Site*

A site in the northern Death Valley (northern Death Valley 1 or NDV-1) (Fig. 1) was selected for this study because of the well-known mineralogy derived from previous data collections, analyses, and field validation. The site has been studied in detail using field mapping[30–33] and a wide variety of remote sensing datasets.[32,34–36] Bedrock consists of Precambrian limestones, dolomites, sandstones and their contact metamorphic equivalents; granitic-composition Mesozoic plutonic rocks (quartz syenite, a quartz monzonite porphyry stock, quartz monzonite dikes, and a granite intrusion), and complexly faulted tertiary volcanic rocks, and volcaniclastic sedimentary rocks interbedded with rhyolite and basalt[33] (Fig. 2). Quaternary deposits include Holocene and Pleistocene fanglomerates, pediment gravels, and alluvium; these have been mapped in reconnaissance,[31] but no linked bedrock/surficial geology studies have been completed. This area underwent several episodes of hydrothermal alteration (Fig. 3): (1) sericite (fine-grained muscovite or illite) and Fe oxide minerals in narrow north-trending mineralized shear zones,[32,33] and (2) slightly broader northwest-trending zones of disseminated quartz, pyrite, sericite, chalcopyrite, and fluorite mineralization [Quart-Sericite-Pyrite (QSP) alteration] $\pm$ Fe oxides occurring in the quartz monzonite porphyry and spatially associated with fine-grained quartz monzonite dikes.[32] There are several small areas of quartz stockwork (silica flooding of the rocks) exposed at the surface in the center of the area. Skarn, composed mainly of brown andradite garnet intergrown with calcite, epidote, and tremolite occurs around the perimeter of the quartz monzonite stock in Precambrian rocks. This is an extremely arid area and

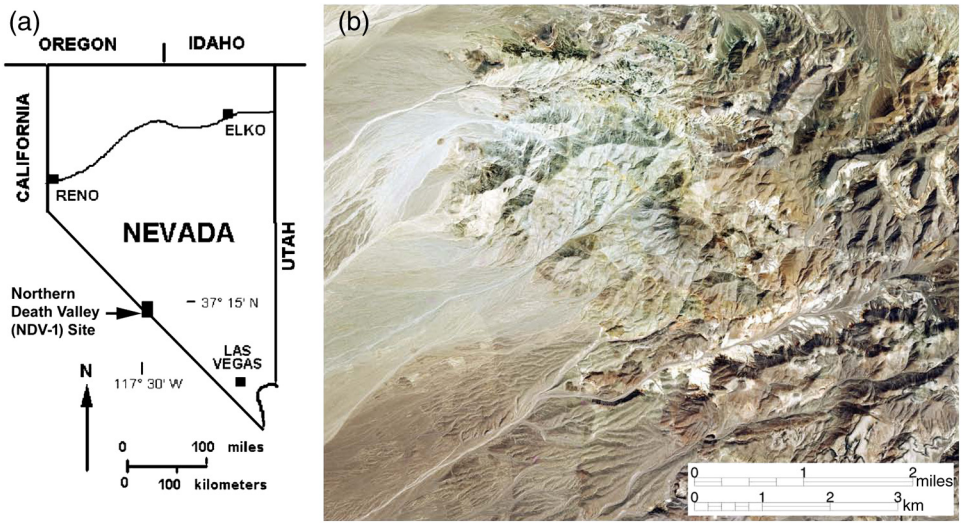

Fig. 1 (a) Northern Death Valley site #1 (NDV-1) location map and (b) true color orthorectified aerial photography. All datasets used in this study were coregistered to the ortho-imagery and USGS digital orthoquad (DOQ) photography.

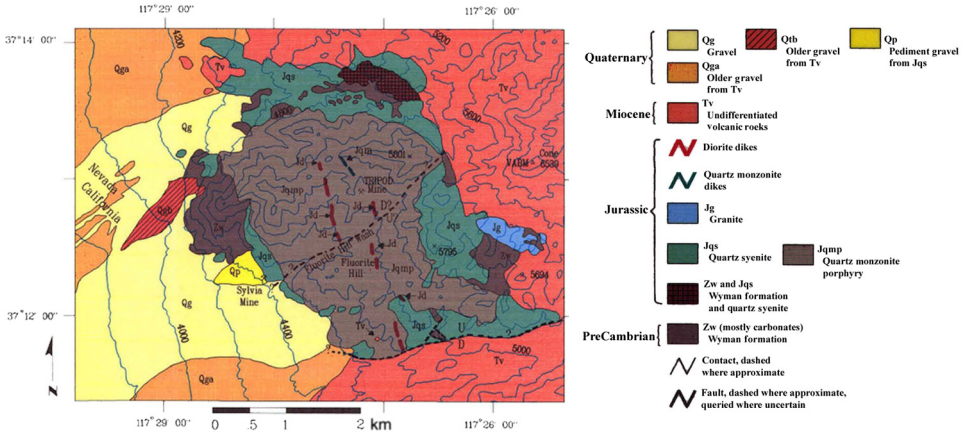

Fig. 2 Geologic map and key produced utilizing traditional field mapping techniques.[34]

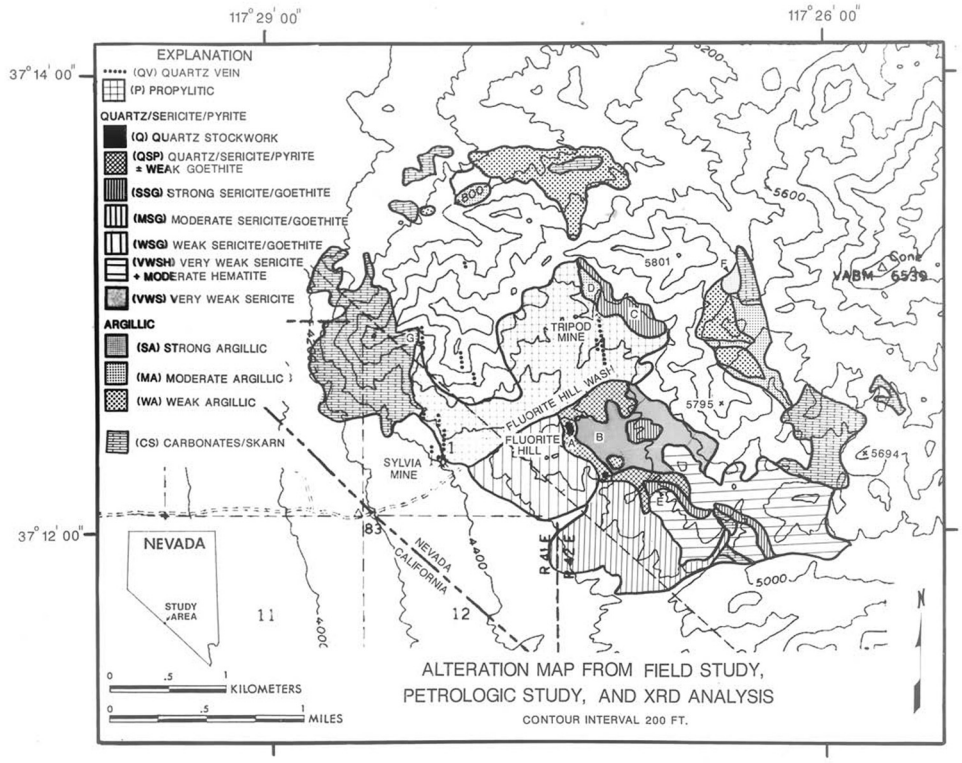

Fig. 3 Alteration map from field study, petrology, and x-ray diffraction analysis.[34]

vegetation coverage is very low. Field observations indicate the presence of small amounts of both green and dry desert shrubs and grasses (typically $< \sim 5$ to 10%).

1.3 *Hyperspectral Imagery Datasets*

AVIRIS is an airborne hyperspectral sensor with 224 bands at 10 nm spectral resolution over the range of 0.4 to 2.5 μm.[37,38] It has been used extensively since 1989 for hyperspectral mineral mapping and other applications.[38] Multiple AVIRIS datasets were acquired for the NDV-1 site between 1989 and 2006. The AVIRIS data used for this investigation were acquired on November 5, 2005. A total of 80 VNIR bands from 0.4 to 1.2 μm and 51 SWIR bands from 2.0 to 2.5 μm at 3.2 m spatial resolution were used in these analyses. The SWIR data between 1.2 and 2 μm were not used as the area is sparsely vegetated and few minerals of interest

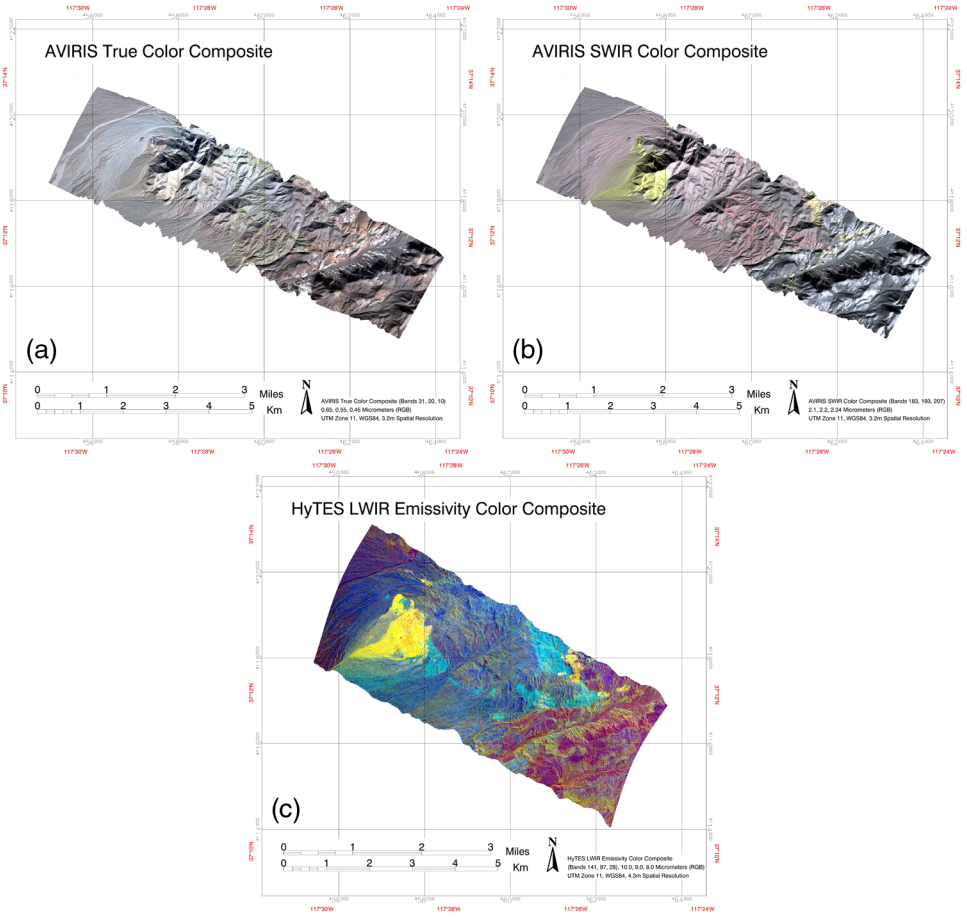

Fig. 4 (a) Airborne visible/infrared imaging spectrometer (AVIRIS) visible to near-infrared (VNIR) reflectance true color image, bands 31, 20, 10 (0.66, 0.55, 0.45 μm) as RGB; (b) AVIRIS shortwave infrared (SWIR) reflectance color composite image, bands 183, 193, 207 (2.1, 2.2, 2.34 μm) as RGB; and (c) hyperspectral thermal emission spectrometer (HyTES) longwave infrared (LWIR) emissivity color composite image, bands 141, 84, 28 (10.0, 9.0, 8.0 μm) as RGB.

in this geologic setting have distinctive absorption features in this region. HyTES is an airborne LWIR hyperspectral sensor with 256 bands at ~17 nm spectral resolution covering the 7.5 to 12.0 μm range.[39] HyTES data were acquired for the NDV-1 site on July 7, 2014, at 4.3 m spatial resolution. Two hundred spectral bands between 8.0 and 11.5 μm were used for this investigation. While the nearly 10-year time difference between the two datasets could potentially negatively affect analyses, this is a very arid area with good bedrock exposure, and spectral-spatial browsing of the imagery indicates that surface changes have been minimal. Figure 4 shows color composite images for the NDV-1 site for the three spectral ranges (VNIR, SWIR, and LWIR).

2 Approaches and Methods

The HSI data for the NDV-1 site were analyzed using a standardized approach [Fig. 5(a)].[40,41] AVIRIS VNIR and SWIR HSI radiance data were converted to reflectance utilizing the Atmospheric Correction Now (ACORN) atmospheric model.[42] This is a MODTRAN-based model requiring only knowledge about the HSI acquisition parameters (sensor, date, time, altitude), site characteristics (latitude and longitude, elevation), and some basic assumptions (atmospheric model, visibility). ACORN adjusts the wavelength calibration as required, calculates the atmospheric water vapor concentration from the radiance spectra, determines reflectance utilizing the measured water vapor and the atmospheric model, masks portions of the spectrum with low signal-to-noise ratios (SNR), and removes residual sensor artifacts—all without any

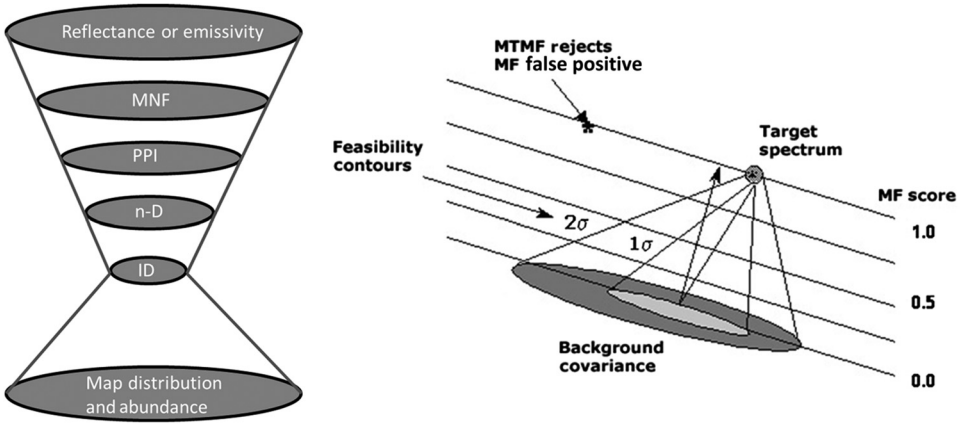

Fig. 5 (a) Standardized hyperspectral imagery (HSI) analysis approach: the HSI data are atmospherically corrected and reduced both spatially and spectrally to just a few key spectra. These are identified, and their spatial distributions and abundances mapped using a variety of methods. Our preferred method is mixture tuned matched filtering (MTMF). (b) MTMF concept showing identification and quantification of a known target spectrum in the presence of a diverse background. Higher matched filter (MF) scores (from 0.0 to 1.0 = 0 to 100% abundance) indicate that there is more of the target spectrum material in the pixel of interest. Lower infeasibility scores [forming 1σ and 2σ (etc.) cones extending from the background to the target] constrain the spectral signature in the context of mixing of the background and target signature. The best spectral matches can be mapped based on meeting the combined criteria of high MF score and low infeasibility score.[41]

supporting ground or atmospheric measurements. The HyTES data were atmospherically corrected using an LWIR atmospheric compensation model, Fast Line-of-sight Atmospheric Analysis of Spectral Hypercubes-Infrared (FLAASH-IR), also requiring no ground information.[43,44] FLAASH-IR calculates a set of trial atmospheric spectra by specifying a three-dimensional grid of atmospheric parameters (surface air temperature, water vapor column density or relative humidity, and an ozone column density scale factor). These parameters are used to determine and modify a MODTRAN model atmosphere temperature at each pixel based on fit to a Plank function. The best-fit atmosphere model is retrieved from selected pixel spectra by minimizing the total variance with respect to both surface temperature and the atmospheric variables. While FLAASH-IR also offers temperature-emissivity (TES) capabilities, for this study, the atmospherically corrected HyTES were converted to emissivity and temperature using a normalized emissivity TES method.[45] Both the AVIRIS reflectance and HyTES emissivity had similar ranges from 0.0 to 1.0, which were scaled from 0 to 10,000 for analysis.

Image-based endmembers and spectral unmixing were then used for both an integrated full-range analysis (332 combined bands) and for independent (modal) analysis of the individual spectral ranges [Fig. 5(a)].[40,41] The selected spectral regions were linearly transformed using the minimum noise fraction (MNF) transform,[46] which conditions n-dimensional data in preparation for determination of endmembers and spectral unmixing.[41] A subset of the MNF data was used to determine the spectrally extreme pixels in each dataset using repeated projections of n-dimensional scatterplots (where n is the number of bands) onto a lower-dimensional subspace and marking the extreme pixels calculated—the pixel purity index (PPI).[41,47] The PPI results were then analyzed using interactive n-dimensional scatterplots to determine vertices, which typically correspond to unique materials—the endmembers. The endmember spectra were visually compared to spectral libraries[7,10,12] to determine key spectral features and identify minerals (AVIRIS) and rock types (HyTES). These were then used in a partial unmixing algorithm, mixture tuned matched filtering (MTMF) [Fig. 5(b)], to map the spatial occurrence and abundance of each endmember for each dataset.[41,48]

MNF is used to segregate noise in the data, determine inherent data dimensionality, and reduce computational requirements for subsequent processing.[41,46] It is equivalent to principal components (PCs) when the noise variance (SNR) is the same in all bands. MNF orders data according to decreasing SNR rather than ordering by variance as for PCs. It divides the data space into two parts, one with large eigenvalues and coherent eigenimages, and the second

with near-unity eigenvalues and noise-dominated images. Only the first part of the MNF-transformed data was used for subsequent analyses, thus segregating signal from noise and reducing the spectral dimensionality of the datasets.

PPI utilizes the concepts of convex geometry to find the spectrally pure or extreme pixels in n-dimensional HSI data, where n is the number of bands.[41,47] The digital number of each pixel in the PPI image corresponds to the number of times that pixel was recorded as extreme (higher PPI = purer). The PPI image is then thresholded to limit the pixels selected for further analysis to only the most extreme (pure) pixels, thus reducing the spatial dimensionality of the data. The remaining pixels, corresponding to endmembers, were interactively visualized using n-dimensional scatterplotting to extract the vertices of the scatterplots,[41] and these were identified using visual inspection and matching to library spectra.[7,10,12]

MTMF is a hybrid partial unmixing algorithm[41,48] utilizing the classical matched filter (MF) statistical detection technique[49,50] used for radio/radar signals in conjunction with a linear mixture model[51] to determine the occurrence and abundance of targets in the presence of a mixed background. The MF vector is calculated by determining the background covariance and then finding an orthogonal vector that maximizes the known target separation from the composite background. MF scores are calculated by projecting data onto the MF vector, giving apparent pixel fractional fill (abundance). MF was designed for radar data, however, where signals are additive. False positives may occur when MF is used for analysis of optical remote sensing data because mixing is a replacement process. MTMF is designed to remedy this MF shortcoming. The mixture tuned part of the MTMF algorithm determines the probability that a given spectrum is a feasible linear mixture of the background and the target. It is measured in concentric equal-probability cones as standard deviations from the MF vector [Fig. 5(b)]. MTMF combines the best attributes of the MF with the feasibility constraints of spectral mixing. It allows both determination of specific materials and estimation of their pixel abundances by calculating two measures: the MF score and an infeasibility score. These two attributes are typically used together in two-dimensional (2-D) scatterplots to determine occurrence and abundance of a particular material at each pixel of a spectral image dataset. The MF score determines the spectral abundance of the material, while the infeasibility score determines whether the measurement is a feasible mixture of background and the target signature. A combination of high MF and low infeasibility score determines the best target match, highlighting feasible mixtures; however, this is somewhat subjective. For the purposes of this research, an MTMF feasibility ratio (MF score/infeasibility score) was used for standardization between the datasets. All data analyzed utilizing MTMF were thresholded to show only the best match (one material per pixel) for MTMF feasibility ratios >0.025.

3 Results

The 2005 AVIRIS SWIR data for the NDV-1 site were previously analyzed utilizing the standardized approach described previously, but with manual MTMF mapping using 2-D scatterplotting thresholds.[40] The current research presents updated SWIR analysis using the same data and the MTMF feasibility ratio approach for more objective mapping and further standardization. It also adds both independent and integrated analysis of the AVIRIS VNIR and SWIR data, and the HyTES LWIR data.

3.1 *Full-Range Integrated Analysis*

Corrected reflectance and emissivity spectral bands from VNIR, SWIR, and LWIR spectral ranges were combined to form a full-range hyperspectral dataset with 332 bands to assess the value of processing and analyzing these as an integrated dataset. Both the AVIRIS and HyTES data were geocorrected using onboard navigation information at their native spatial resolutions (3.2 and 4.3 m, respectively) and then further georeferenced to 1 m spatial resolution orthophotography utilizing ground control points (GCPs), Delaunay triangulation, and nearest-neighbor resampling. Residual errors utilizing 350 GCPs for AVIRIS were on the order of 3 m (1 AVIRIS pixel) and with 54 GCPs for HyTES, 4 m (1 HyTES pixel). The VNIR, SWIR, and

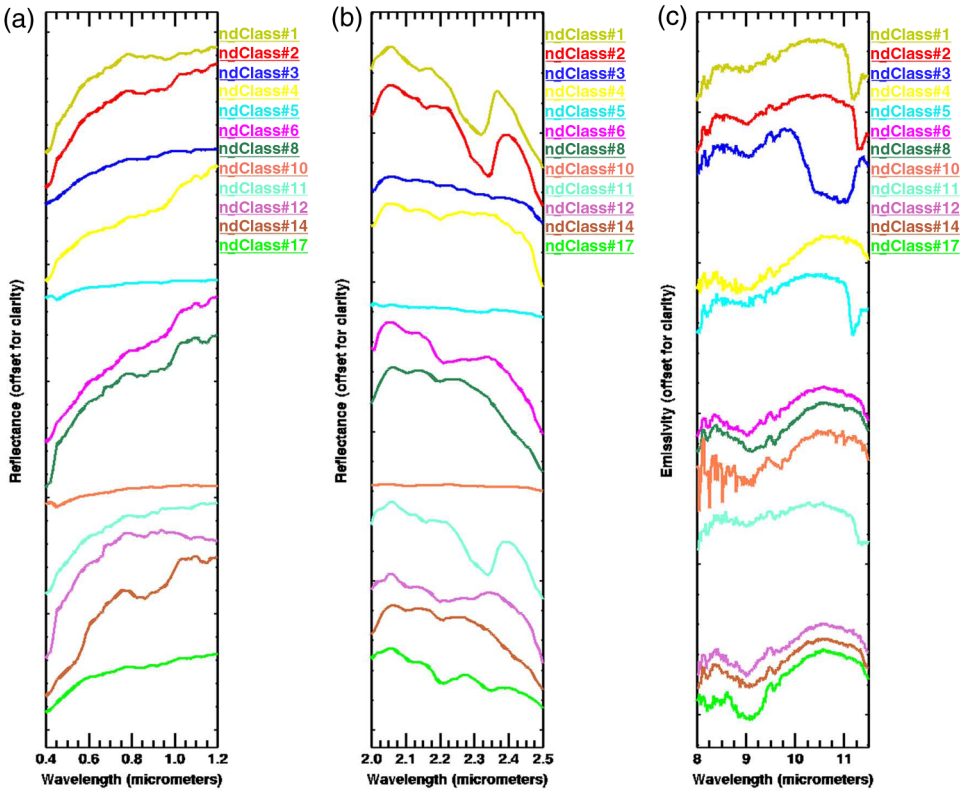

Fig. 6 Selected combined AVIRIS/HyTES endmembers extracted from the data using the standardized approach: (a) AVIRIS VNIR, (b) AVIRIS SWIR, and (c) HyTES LWIR. Note that while spectral plots shown are broken into the three wavelength regions for scaling, they are in fact continuous VNIR-SWIR-LWIR endmembers. The colors and names track across the three plots (Table 1 and Fig. 7).

LWIR data were stacked to form a datacube at the uniform 1 m grid size. The combined dataset was then analyzed using the endmember extraction approach across all bands (Fig. 6) and partial unmixing utilizing the MTMF and MTMF feasibility ratio approach (Fig. 7). The constant ratio threshold of 0.025 was used to map the spatial distribution of the predominant endmember at each pixel. Using assemblages of materials (based on full-range analysis) to designate classes is probably more similar to the way a geologist maps than typical single wavelength range HSI mineral mapping. The integrated mapping does appear to bring out some associations that are not easily observable in individual ranges (Figs. 6 and 7, Table 1). For example, a mixed carbonate/silica fan classified as ndClass#17 and marked as A in Fig. 7 is clearly discriminated from other fans with mostly carbonates (calcite classified as ndClass#2) and marked as B. Unfortunately, however, other areas of unrelated alteration (marked as C in Fig. 7) are also mapped as part of ndClass#17. These areas generally correspond with field mapped areas of QSP alteration $\pm$goethite (Fig. 2). The integrated data also illustrate what can happen when spectral features are obscured in one spectral range because of calibration issues or problems with shadows or temperature differences. For example, dolomite mapped as ndClass#5, marked as D in Fig. 7, has a strong 11.2 μm emissivity minimum in the LWIR (HyTES) data [Fig. 6(c)], but the expected corresponding dolomite feature near 2.32 μm is very weak or does not appear in the SWIR (AVIRIS) portion of the endmember spectrum [Fig. 6(a)], apparently because location D occurs in a shadowed area. Fully illuminated carbonates are correctly mapped by the integrated full-range data as calcite at locations E and F as ndClass#2 and ndClass#11, and dolomite at location G as ndClass#1, respectively, in Fig. 7 based on joint occurrence of the SWIR absorption feature near 2.34 or 2.32 μm and the LWIR emissivity minimum near 11.3 or 11.2 μm, respectively [Figs. 6(b) and 6(c)]. A similar situation occurs for ndClass#9, where there is a dolomite absorption feature in the SWIR at 2.32 μm, but no corresponding LWIR dolomite feature near 11.2 μm (not shown).

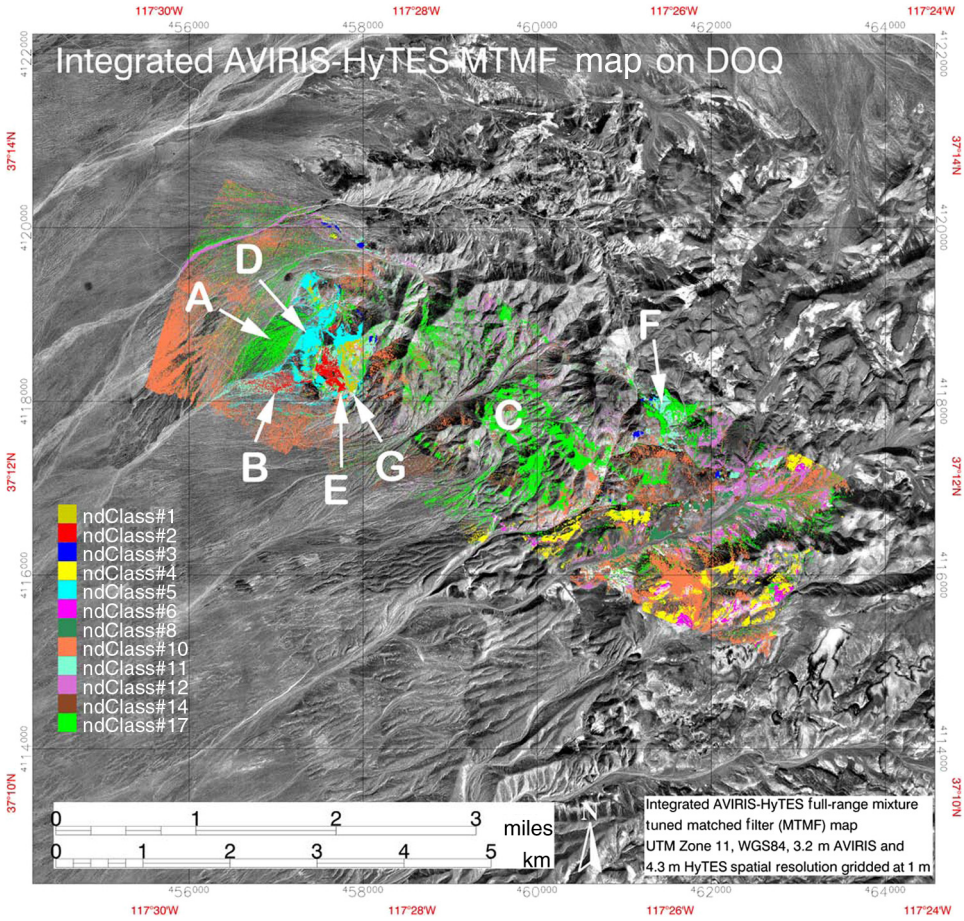

Fig. 7 AVIRIS-HyTES combined full-range MTMF mapping results using the integrated endmembers shown in Fig. 6. Comparison to Fig. 3 shows good discrimination of alteration; however, comparison to Fig. 2 indicates that this approach does not perform well for lithology (geology). Locations and endmembers: A and C, ndClass#16; B, ndClass#2; D, ndClass#5; E, ndClass#2; F, ndClass#11; G, ndClass#1 (see Fig. 6).

The major problem with the integrated analysis approach is that often the causes of class differences are hard to determine and the results are difficult to interpret. It may not always be possible to assign multirange absorption and/or emissivity features to the physical and/or chemical phenomenology or specific rock units (Table 1, Fig. 7). Figure 7 shows that this approach also appears to suppress individual lithologies expressed in the LWIR data [Fig. 4(c)]. Note, for example, that the quartz syenite rock unit, clearly seen as the light blue unit in the HyTES data [Figs. 2 and 4(c)], is not mapped as a distinct unit utilizing the integrated dataset. The advantages of the integrated full-range analysis approach are that it requires less spectroscopic knowledge to get started, offers streamlined analysis, and captures the inherent data complexity. Problems include mapping errors associated with materials that have slightly different reflectance or emissivity characteristics because of shadows and/or uncorrected temperature differences, respectively, along with possible residual sensor or atmospheric correction errors.

3.2 *Independent Modal Hyperspectral Imagery Data Analysis*

The VNIR and SWIR reflectance data and LWIR emissivity data were also used independently to determine key endmembers in each spectral range using the endmember extraction and MTMF mapping approach. Materials were identified based on comparison of specific spectral absorption features to spectral libraries.[7,10,12] Partial unmixing utilizing MTMF was used individually for each range to map the distribution and abundance of selected endmembers. Results presented here show only the predominant material at each pixel, extracted using the MTMF

Table 1 Interpreted mineralogy from each spectral range for selected classes extracted from integrated dataset.

Combined class	Image color (Fig. 7)	VNIR spectral ID	SWIR spectral ID	LWIR spectral ID
ndClass#1	Dark yellow	Weak Fe	Dolomite	Dolomite
ndClass#2	Red	Goethite	Calcite	Calcite
ndClass#3	Blue	None	None	Calc-silicate
ndClass#4	Yellow	Weak Fe	Weak clay	Silicate
ndClass#5	Cyan	None	Very weak dolomite	Dolomite
ndClass#6	Magenta	Weak Fe	Silica	Silicate
ndClass#8	Sea green	Goethite	Clay	Silicate
ndClass#10	Orange	None	Very weak clay	Silicate
ndClass#11	Aquamarine	None	Calcite	Calcite
ndClass#12	Orchid	Unknown	Weak clay	Silicate
ndClass#14	Dark sienna	Hematite	Weak clay	Silicate
ndClass#17	Green	Weak Fe	Muscovite	Silicate/quartz

VNIR, visible to near-infrared; SWIR, shortwave infrared; LWIR, longwave infrared.

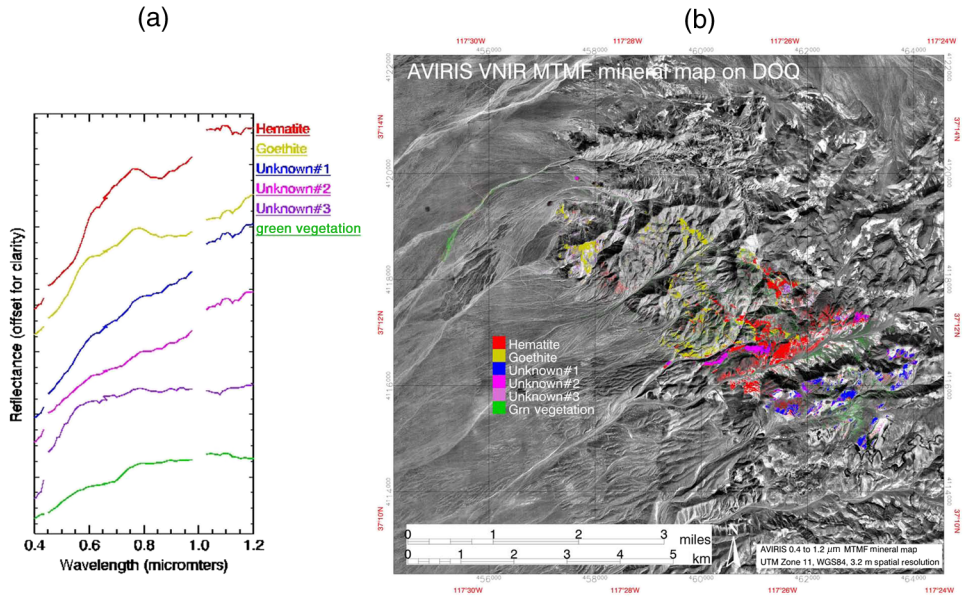

Fig. 8 (a) AVIRIS VNIR endmembers extracted from the data using the standardized approach and (b) AVIRIS VNIR mineral mapping results overlain on USGS DOQ.

feasibility ratio with a constant value of 0.025. The VNIR results principally show the distribution of iron oxides (hematite and goethite), identified based on key absorption features near 0.86 and 0.93 μm, respectively, along with some areas that need further validation (unknown minerals based only on VNIR spectral signatures; Fig. 8). Minor green vegetation (~1.3% overall) was also mapped. The SWIR analysis (Fig. 9) mapped calcite (limestone) and dolomite, identified based on key absorption features near 2.34 and 2.32 μm, respectively; mica (muscovite/sericite) based on a combination of key features near 2.2 and 2.36 μm; silica identified using a broad absorption feature near 2.2 μm; zeolites based on overall SWIR spectral shape (volcanic

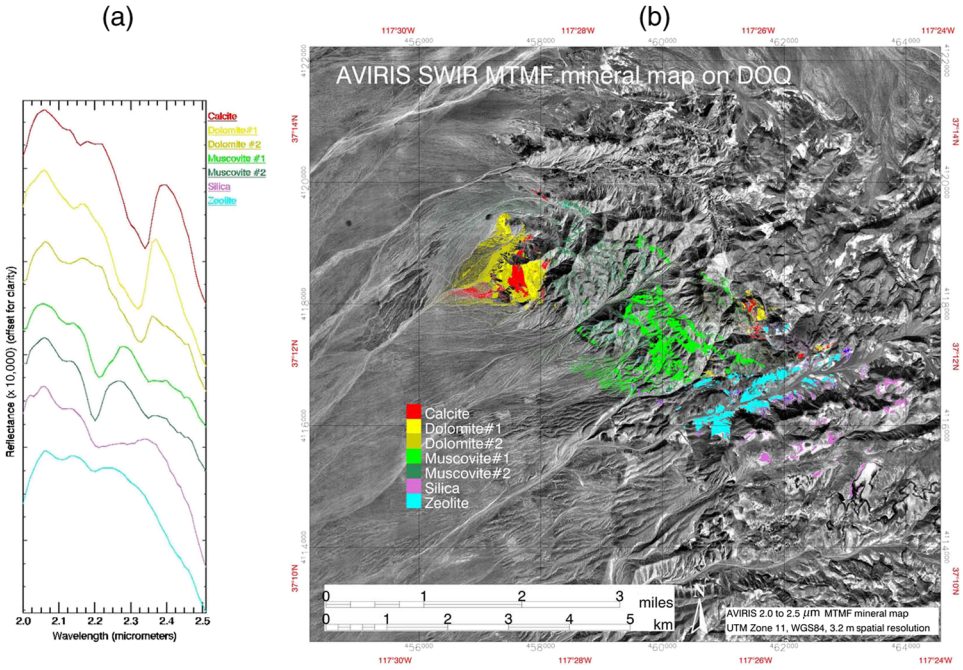

Fig. 9 (a) AVIRIS SWIR endmembers extracted from the data using the standardized approach and (b) AVIRIS SWIR mineral mapping results overlain on USGS DOQ.

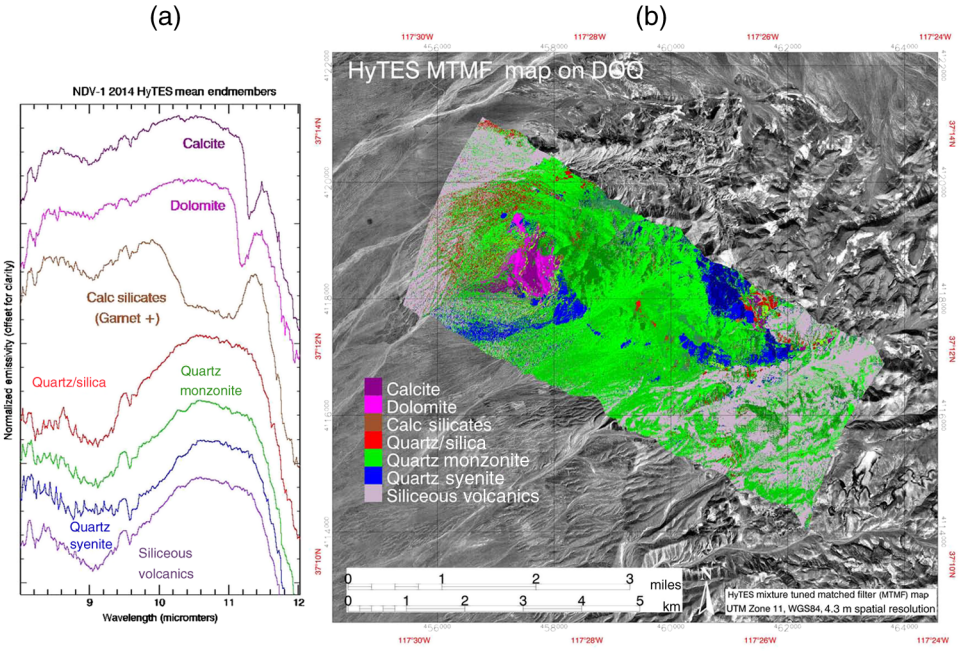

Fig. 10 (a) HyTES LWIR endmembers extracted from the data using the standardized approach and (b) HyTES LWIR MTMF mapping results overlain on USGS DOQ.

rocks); and dry vegetation (~1.5% overall, not shown). The HyTES data discriminated various rock types including quartz syenite, quartz monzonite, and siliceous volcanic rocks identified based on unique, slightly shifted emissivity minima features near 9.0 μm (Fig. 10). Limestone and dolomite were identified based on features near 11.2 and 11.3 μm, respectively [Fig. 10(a)]. Calc-silicate alteration (andradite garnet skarn) was identified based on a broad emissivity minimum spanning the 10.4 to 11.1 μm range [Fig. 10(a)]. Silica stockworks and other silicification were determined by the presence of the quartz restrahlen features near 8.5 and 9.0 μm

Table 2 Combined carbonate classification scheme using logical operators applied to modal spectral identifications.

Mode	Modal spectral identifications (carbonates)			
AVIRIS VNIR	—	—	—	Goethite AND
AVIRIS SWIR	Calcite	Dolomite	Calcite OR Dolomite	Calcite OR Dolomite
Operator	OR	OR	OR	OR
HyTES LWIR	Calcite	Dolomite	Calcite OR Dolomite	Calcite OR Dolomite
Combined classification	1. Combined calcite	2. Combined dolomite	3. Combined carbonate	4. Altered carbonate

AVIRIS, airborne visible/infrared imaging spectrometer; HyTES, hyperspectral thermal emission spectrometer.

[Fig. 10(a)]. Rock type names were assigned based on their spectral signatures and comparison to known lithologies (Fig. 2). Compare the HyTES MTMF map (Fig. 10) to the geologic map (Fig. 2) and note the close correspondence of the various rock types.

These results demonstrate the different identification and mapping capabilities of each wavelength range. Independently analyzing each HSI mode provides the advantage of clear ties between the mapping and physical and chemical properties. VNIR and SWIR do not usually map rock type (lithology) in the classical sense (with the exception of limestone and dolomite in the SWIR). Instead, in this case, they principally map crosscutting mineralogy associated with hydrothermal alteration (Fig. 3). The LWIR map, which principally shows differences between primary rock-forming silicates, more closely resembles the geologic map (Fig. 2). Comparison of the material maps from the different modes reveals complex overlap, indicating that multiple materials/processes exist in many areas. Thus, combination or integration of the results is necessary to produce the best surface materials maps.

3.3 *Directed Modal Combined Results*

The approach used to integrate the individual VNIR-SWIR-LWIR results was to utilize class merging, masking, and logical operators to combine classes produced during the independent modal analyses of the multiple ranges. Use of multispectral advanced spaceborne thermal emission and reflection radiometer remote sensing data and logical operators has been demonstrated by the U.S. Geological Survey (USGS) for mapping specific spectral absorption features associated with hydrothermal alteration.[52,53] The approach described here is similar; however, MTMF mapping results for individual spectral regions were combined utilizing selected logical

Table 3 Combined classification using logical operators applied to modal spectral identifications.

Mode	Modal spectral identifications (non-carbonates)						
AVIRIS VNIR	—	Goethite AND	Hematite AND	Not Fe-oxides AND	—	—	—
AVIRIS SWIR	—	Muscovite	Muscovite	Muscovite	—	—	—
Operator		AND	AND				
HyTES LWIR	Qtz monzonite	Qtz monzonite	Qtz monzonite	—	Quartz/silica	Calc-silicates	Quartz syenite
Combined classification	5. Quartz monzonite	6. Altered Qtz Monz#1	7. Altered Qtz Monz#2	8. Muscovite	9. Qtz/silica	10. Calc-silicates	11. Quartz syenite

operators based on known geologic and spectroscopic constraints for the NDV-1 site. These fuse modal analyses to reduce variability, reveal additional detail, and clarify mineral assemblages and rock associations (Tables 2 and 3, Figs. 11 and 12).

Close examination of the SWIR mineral mapping of the carbonate units [calcite and dolomite spectra, Fig. 11(a)] reveals that AVIRIS had some difficulties identifying these materials in shadowed areas [Fig. 11(b)]. Additionally, HyTES mapping appeared to be less sensitive in low abundance carbonate areas [Figs. 11(c) and 11(d)]. Thus, in some locations, materials had the SWIR carbonate features, but no LWIR carbonate features and vice versa. Combining

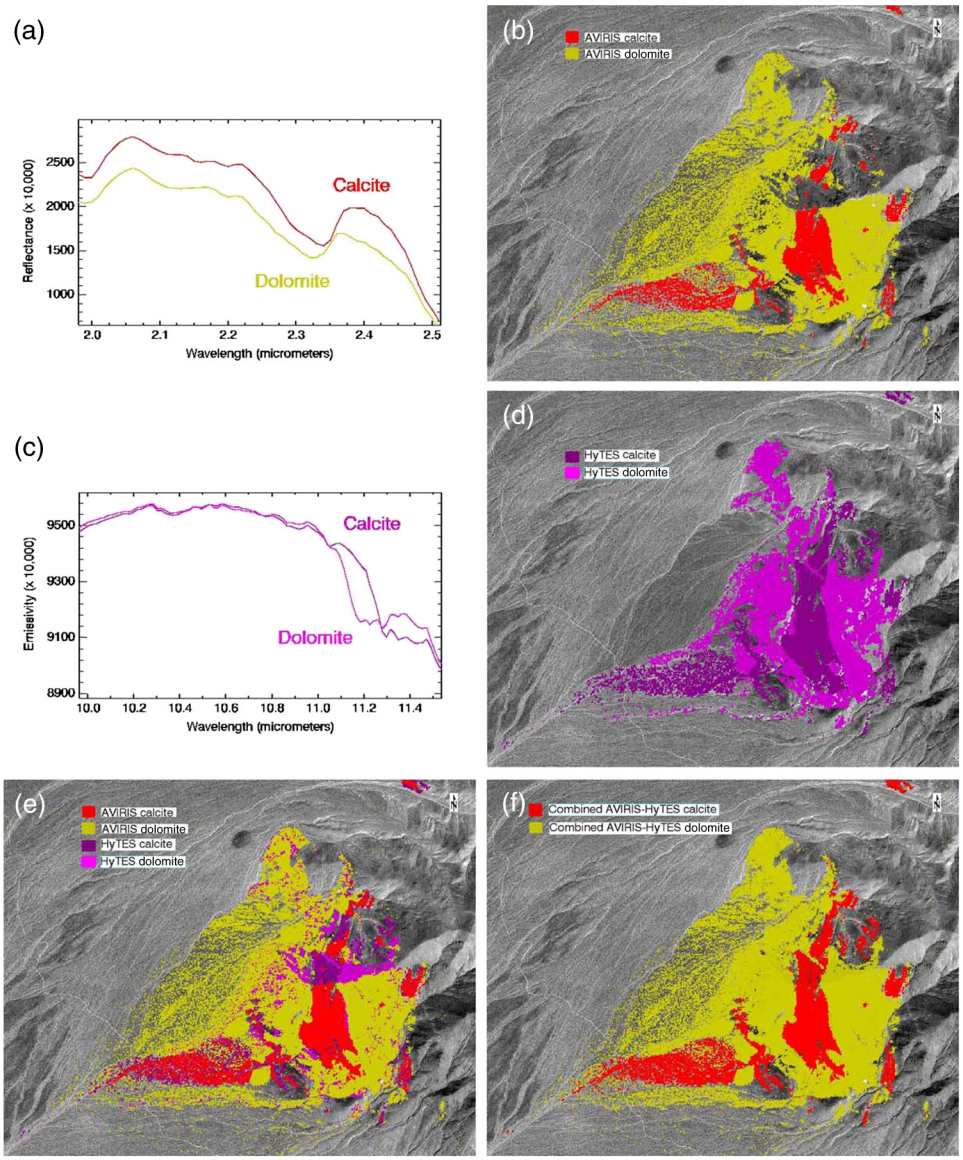

Fig. 11 (a) AVIRIS carbonate image endmembers dolomite and calcite based on their SWIR absorption features near 2.32 and 2.34 μm, respectively, (b) MTMF SWIR mineral map subset showing AVIRIS carbonate mapping, (c) HyTES carbonate image endmembers dolomite and calcite based on their LWIR emissivity minima near 11.2 and 11.3 μm, respectively, (d) MTMF LWIR mineral map subset showing HyTES carbonate mapping. Image (e) shows combined results. AVIRIS calcite and dolomite mapped as red and yellow, respectively, and HyTES carbonates [where not mapped by AVIRIS, compare (b) and (d)], in shades of purple. Image (f) shows final combined map of all mapped calcite and dolomite. HyTES-only mapped carbonates shown in purple in (e) were added to AVIRIS-only results in (b) to achieve (f). Note removal of mapping discontinuity at ridgeline in shadowed areas. All mineral maps overlain on USGS DOQ.

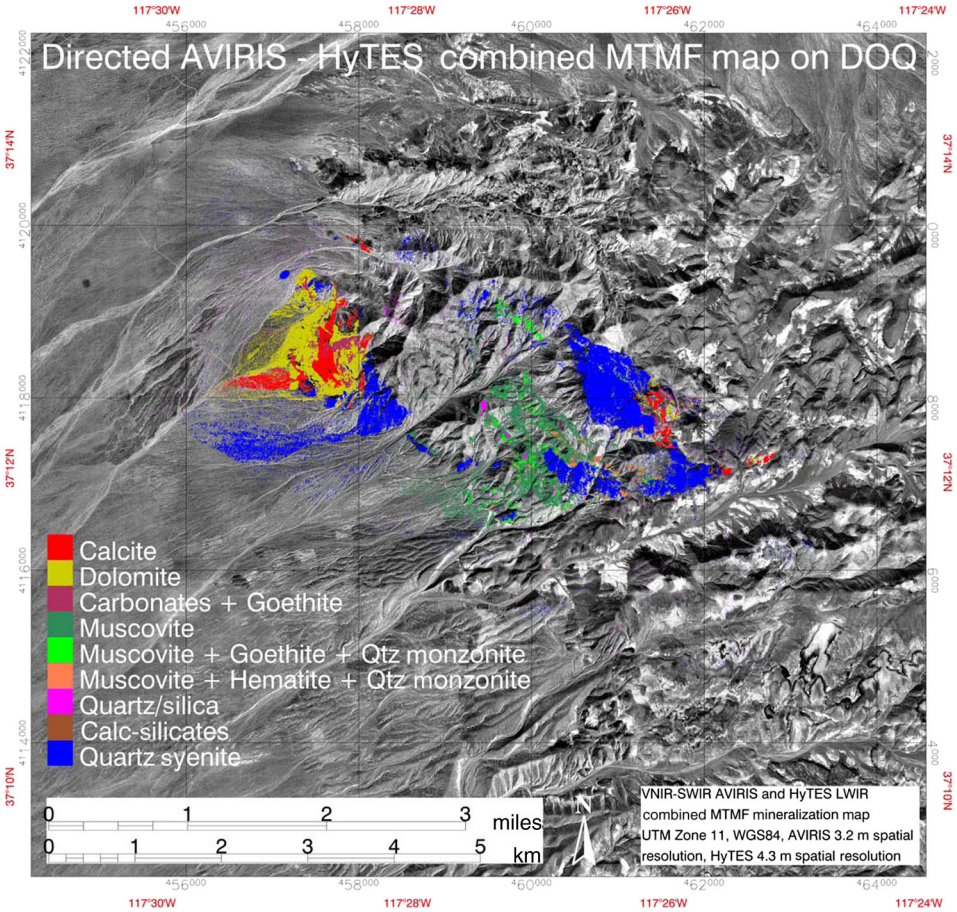

Fig. 12 Integrated image map from directed combined analysis of individual VNIR-SWIR-LWIR material maps showing key alteration assemblages for the NDV-1 site overlain on USGS DOQ.

the two MTMF classifications using a logical OR (mapping locations where either AVIRIS or HyTES found carbonates) produced a more coherent map of the carbonate units that did not have discontinuities at terrain boundaries [Table 2, Figs. 11(e) and 11(f)].

A similar approach was taken toward mapping individual lithologies and selected mineral assemblages. Geologic context was used to combine similar materials and to generate mineral assemblages related to hydrothermal alteration (Tables 2 and 3, Fig. 12). Variability in spectral units for areas recognized by their HyTES LWIR emissivity signatures and named as quartz syenite, quartz monzonite, or silicic volcanic rock based on comparison to known geology were combined into individual discrete rock units. Areas of similar endmember spectra were merged using the logical OR operator to create individual classification masks. Note the unambiguous mapping of the quartz syenite intrusive phase derived from the HyTES data based on its reduced silica content relative to the quartz monzonite unit (compare Figs. 10 and 12 to the geologic map, Fig. 2). This is particularly important for mapping hydrothermal alteration, as significant amounts of alteration at this site occur along the boundaries of or within the quartz syenite intrusive phase.

Alteration assemblages were principally identified based on the joint occurrence of VNIR-determined minerals (Fe oxides) and mica (muscovite/sericite) in the LWIR-defined quartz monzonite rock unit using a logical AND operator (Table 3). SWIR-mapped muscovite/sericite alteration without additional alteration minerals was mapped as one alteration type (muscovite; Table 3, Fig. 12). Other occurrences of muscovite associated with Fe oxides were divided into two types based on the joint occurrence of either hematite or goethite in VNIR mapping association (Table 3, Fig. 12). VNIR-mapped goethite areas are also present in SWIR-LWIR mapped carbonates, crosscutting calcite/dolomite boundaries, possibly indicating additional alteration (Table 2, Fig. 12). Areas of calc-silicates and silicification were determined solely from

their LWIR signatures (Table 3). Their location in geologic context at the carbonate/intrusive contact based on combined wavelength mapping (Fig. 12) indicates that they are carbonates altered to skarn. These areas were field validated as principally andradite garnet. The occurrence of silicification mapped using the LWIR (Table 3, Fig. 12) indicates likelihood of intense alteration, also field verified as quartz stockworks. Together, the VNIR-SWIR-LWIR combined modal mapping results lead to improved application-specific characterization and mapping that could not be accomplished using a single spectral range (Figs. 8–12). The advantage of this approach is that the analyses can be tailored to specific materials of interest. This however requires subject-matter expertise that must be applied to the individual datasets in order to combine them in appropriate ways that make sense in terms of geologic (or other) context.

4 Summary and Conclusions

Full-range (0.4 to 12 μm) HSI data of a site in northern Death Valley, California and Nevada, were used to improve geologic mapping and characterization and mapping of hydrothermal alteration. Integrated simultaneous analysis of HSI data for the NDV-1 site using the full VNIR-SWIR-LWIR spectral range made it possible to map materials with spectral features in multiple wavelength regions. The integrated mapping highlights subtle associations that are not easily observable by mapping the spectrally predominant material in individual ranges. The main advantage of this approach is efficient processing (reduced computation and data volumes) through streamlining of the processing flow. Results, however, were difficult to understand and relate to surface properties and geologic processes. In this case, the fully integrated analysis did not fully capture valuable geologic information for basic lithologic and alteration mapping, providing more of a broad picture view.

Independent analysis of the VNIR and SWIR AVIRIS and HyTES LWIR hyperspectral data for each spectral range produced information-rich spatial patterns. Complex overlap occurs between results from the different spectral regions. This was resolved by combining results from the multiple modalities utilizing specific spectral features and class merging, masking, and logical operators in geologic context. Spectral endmembers and spatial material distributions could then be directly related to physiochemical properties and geologic processes. This accomplished improved characterization and mapping that could not be performed using a single spectral range. The approach, however, required application-specific geologic expertise and manual intervention.

The full-range results illustrate that integrated analysis provides advantages over use of just one spectral range, leading to improved understanding of the distribution of geologic units and alteration. We continue to explore both the integrated spectral bands (full-range) approach and the multimodal classifications. There are several outstanding issues, including clarification of spatial constraints imposed by different pixel resolutions and slight misalignment of different wavelength regions/modes. Temporal decorrelation is also a concern, as most multimodal data are not collected simultaneously. This can be addressed by acquiring and analyzing temporally consistent datasets acquired at the same time on the same platform with similar spatial resolution.

Acknowledgments

Airborne visible/infrared imaging spectrometer and hyperspectral thermal emission spectrometer data for the northern Death Valley 1 site were acquired and calibrated to radiance by the Jet Propulsion Laboratory. Steve Adler-Golden (Spectral Sciences Inc.) is acknowledged for his assistance in understanding the FLAASH-IR atmospheric compensation approach for longwave infrared hyperspectral imagery data. Use of brand names in this manuscript does not indicate endorsement by the U.S. government.

References

1. H. H. Adler, "Some basic considerations in the application of infrared spectroscopy to mineral analysis," *Econ. Geol.* **58**(4), 558–568 (1963).

2. G. R. Hunt, "Spectral signatures of particulate minerals in the visible and near infrared," *Geophysics* **42**(3), 501–513 (1977).
3. G. R. Hunt and R. P. Ashley, "Spectra of altered rocks in the visible and near infrared," *Econ. Geol.* **74**(7), 1613–1629 (1979).
4. S. J. Gaffey, "Spectral reflectance of-carbonate minerals in the visible and near infrared (0.35–2.55 microns): calcite, aragonite, and dolomite," *Am. Mineral.* **71**, 151–162 (1986).
5. J. W. Salisbury and L. S. Walter, "Thermal infrared (2.5–13.5 micrometers) spectroscopic remote sensing of igneous rock types on particulate planetary surfaces," *J. Geophys. Res.* **94**(B7), 9192–9202 (1989).
6. R. N. Clark et al., "High spectral resolution reflectance spectroscopy of minerals," *J. Geophys. Res.* **95**, 12653–12680 (1990).
7. J. W. Salisbury et al., *Infrared (2.1–25 micrometers) Spectra of Minerals*, p. 294, Johns Hopkins University Press, Baltimore, MD (1991).
8. R. N. Clark, "Spectroscopy of rocks and minerals, and principles of spectroscopy," Chapter 1 in *Manual of Remote Sensing, Volume 3, Remote Sensing for the Earth Sciences*, pp. 3–58, John Wiley and Sons, New York (1999).
9. T. Cudahy, "Infrared spectroscopy in geochemistry, exploration geochemistry, and remote sensing: Penelope King, Michael Ramsey, and Gregg Swayze, editors. Mineralogical Association of Canada, Short Course Series Volume 33. 2004. 284 Pp. ISBN 0-921294-33-6," *Econ. Geol.* **100**(8), 1663–1664 (2005).
10. R. N. Clark et al., "USGS digital spectral library splib06a," US Geological Survey Digital Data Series 231, 2007, http://speclab.cr.usgs.gov/spectral.lib06 (31 August 2015).
11. G. A. Swayze et al., "Mapping advanced argillic alteration at Cuprite, Nevada, using imaging spectroscopy," *Econ. Geol.* **109**(5), 1179–1221 (2014).
12. A. M. Baldridge et al., "The ASTER spectral library version 2.0," *Remote Sens. Environ.* **113**, 711–715 (2009).
13. A. F. H. Goetz et al., "Imaging spectrometry for earth remote sensing," *Science* **228**, 1147–1153 (1985).
14. F. D. van der Meer et al., "Multi- and hyperspectral geologic remote sensing: a review," *Int. J. Appl. Earth Obs. Geoinf.* **14**, 112–128 (2012).
15. A. B. Kahle and A. F. H. Goetz, "Mineralogic information from a new airborne thermal infrared multispectral scanner," *Science* **222**(4619), 24–27 (1983).
16. A. R. Gillespie, A. B. Kahle, and F. D. Palluconi, "Mapping alluvial fans in Death Valley, California, using multichannel thermal infrared images," *Geophys. Res. Lett.* **11**, 1153–1156 (1984).
17. S. J. Hook et al., "The MODIS/ASTER airborne simulator (MASTER)—a new instrument for earth science studies," *Remote Sens. Environ.* **76**(1), 93–102 (2001).
18. S. J. Hook, "The combined use of multispectral remotely sensed data from the short wave infrared (SWIR) and thermal infrared (TIR) for lithological mapping and mineral exploration," in *Proc. of Fifth Australasian Remote Sensing Conf.*, Vol. 1, pp. 371–380 (1990).
19. M. Abrams, E. Abbot, and A. B. Kahle, "Combined use of visible, reflected infrared, and thermal infrared images for mapping Hawaiian lava flows," *J. Geophys. Res.* **96**(B1), 475–484 (1991).
20. L. C. Rowan, J. C. Mars, and C. J. Simpson, "Lithologic mapping of the Mordor, NT, Australia ultramafic complex by using the advanced spaceborne thermal emission and reflection radiometer (ASTER)," *Remote Sens. Environ.* **99**, 105–126 (2005).
21. L. E. Kirkland et al., "First use of an airborne thermal infrared hyperspectral scanner for compositional mapping," *Remote Sens. Environ.* **80**, 447–459 (2002).
22. M. J. Abrams, S. Hook, and M. C. Abrams, "Imaging spectrometry in the thermal infrared," in *Imaging Spectrometry: Basic Principles and Prospective Applications*, F. Van der Meer and S. M. de Jong, Eds., pp. 283–306, Springer, New York (2011).
23. T. J. Cudahy et al., "Mapping porphyry-skarn alteration at Yerington, Nevada, using airborne hyperspectral VNIR-SWIR-TIR imaging data," in *Proc. IGARSS*, Vol. 2, pp. 631–633 (2001).
24. T. Bowers, "Analysis of VIS-LWIR hyperspectral image data for detailed geologic mapping," *Proc. SPIE* **4725**, 116–127 (2003).

25. R. G. Vaughan and W. M. Calvin, "Synthesis of high-spatial resolution hyperspectral VNIR/SWIR and TIR image data for mapping weathering and alteration minerals in Virginia City, Nevada," in *IEEE Proc.*, pp. 1296–1299 (2004).
26. F. A. Kruse, M. L. McDowell, and S. R. Cone, "Combined analysis of visible-near infrared (VNIR), shortwave infrared (SWIR), and longwave infrared (LWIR) imaging spectrometer data," presented at *Proc. Hyperspectral Imaging and Sounding of the Environment*, 1–4 March 2015, Lake Arrowhead, California, Paper# HW3B.1, Optical Society of America, Washington, DC (2015).
27. M. L. McDowell and F. A. Kruse, "Integrated visible to near infrared, short wave infrared, and long wave infrared spectral analysis for surface composition mapping near Mountain Pass, California," *Proc. SPIE* **9472**, 94721C (2015).
28. S. R. Cone, F. A. Kruse, and M. L. McDowell, "Exploration of integrated visible to near-, shortwave-, and longwave-infrared (full range) hyperspectral data analysis," *Proc. SPIE* **9472**, 94721D (2015).
29. F. A. Kruse, "Comparative analysis of airborne visible/infrared imaging spectrometer (AVIRIS) and hyperspectral thermal emission spectrometer (HyTES) longwave infrared (LWIR) hyperspectral data for geologic mapping," *Proc. SPIE* **9472**, 94721F (2015).
30. J. P. Albers and J. H. Stewart, "Geology and mineral deposits of Nevada," *Nev. Bur. Mines Geol. Bull.* **78**, 80 (1972).
31. B. Moring, "Reconnaissance surficial geologic map of northern Death Valley California and Nevada," Miscellaneous Field Studies Map MF1770, U.S. Geological Survey, Washington, D.C. (1986).
32. F. A. Kruse, "Use of airborne imaging spectrometer data to map minerals associated with hydrothermally altered rocks in the northern Grapevine Mountains, Nevada and California," *Remote Sens. Environ.* **24**(1), 31–51 (1988).
33. C. T. Wrucke et al., "Mineral resources and mineral resource potential of the Little Sand Spring Wilderness Study Area, Inyo County, California," U.S. Geological Survey Open File Report 84-557, p. 20, U.S. Geological Survey, Washington, D.C. (1984).
34. F. A. Kruse, A. B. Lefkoff, and J. B. Dietz, "Expert system-based mineral mapping in northern Death Valley, California/Nevada using the airborne visible/infrared imaging spectrometer (AVIRIS)," *Remote Sens. Environ.* **44**, 309–336 (1993).
35. F. A. Kruse, J. W. Boardman, and J. F. Huntington, "Fifteen years of hyperspectral data: northern Grapevine Mountains, Nevada," in *Proc. of the 8th JPL Airborne Earth Science Workshop*, pp. 247–258 (1999).
36. F. A. Kruse, J. W. Boardman, and J. F. Huntington, "Evaluation and validation of EO-1 Hyperion for mineral mapping," *IEEE Trans. Geosci. Remote Sens.* **41**(6), 1388–1400 (2003).
37. W. M. Porter and H. E. Enmark, "System overview of the airborne visible/infrared imaging spectrometer (AVIRIS)," *Proc. SPIE* **834**, 22–31 (1987).
38. R. Green, "AVIRIS and related 21st century imaging spectrometers for earth and space science," in *High Performance Computing in Remote Sensing*, A. J. Plaza and C.-I. Chang, Eds., pp. 335–358, Chapman and Hall/CRC Press, Boca Raton, Florida (2007).
39. S. Hook, W. Johnson, and M. Abrams, "NASA's hyperspectral thermal emission spectrometer (HyTES)," in *Thermal Infrared Remote Sensing*, C. Kuenzer and S. Dech, Eds., pp. 93–115, Springer, Netherlands (2013).
40. F. A. Kruse and S. L. Perry, "Improving multispectral mapping by spectral modeling with hyperspectral signatures," *J. Appl. Remote Sens.* **3**(1), 033504 (2009).
41. J. W. Boardman and F. A. Kruse, "Analysis of imaging spectrometer data using N-dimensional geometry and a mixture-tuned matched filtering (MTMF) approach," *IEEE Trans. Geosci. Remote Sens.* **49**(11), 4138–4152 (2011).
42. F. A. Kruse, "Comparison of ATREM, ACORN, and FLAASH atmospheric corrections using low-altitude AVIRIS data of Boulder, Colorado," presented at *Proc. of 13th JPL Airborne Geoscience Workshop*, 31 March–2 April 2004, Pasadena, California, JPL Publication 05-3, Jet Propulsion Laboratory, Pasadena, CA (2004).
43. S. M. Adler-Golden et al., "Long-wave infrared surface reflectance spectra retrieved from Telops Hyper-Cam imagery," *Proc. SPIE* **9088**, 90880U (2014).

44. S. M. Adler-Golden and P. Conforti, "Emissivity retrieval in LWIR hyperspectral desert scenes," presented at *Proc. of Hyperspectral Imaging and Sounding of the Environment*, 1–4 March 2015, Lake Arrowhead, California, Paper# HT3B.2., Optical Society of America, Washington, DC (2015).
45. P. S. Kealy and S. J. Hook, "Separating temperature and emissivity in thermal infrared multispectral scanner data: implications for recovering land surface temperatures," *IEEE Trans. Geosci. Remote Sens.* **31**(6), 1155–1164 (1993).
46. A. A. Green et al., "A transformation for ordering multispectral data in terms of image quality with implications for noise removal," *IEEE Trans. Geosci. Remote Sens.* **26**(1), 65–74 (1988).
47. J. W. Boardman, "Automated spectral unmixing of AVIRIS data using convex geometry concepts," in *Summaries, Fourth JPL Airborne Geoscience Workshop*, pp. 11–14, JPL Publication 93-26, Pasadena, CA (1993).
48. J. W. Boardman, "Leveraging the high dimensionality of AVIRIS data for improved sub-pixel target unmixing and rejection of false positives: mixture tuned matched filtering," in *Summaries of the Seventh Annual JPL Airborne Geoscience Workshop*, Jet Propulsion Laboratory, Pasadena, CA (1998).
49. D. O. North, "An analysis of the factors which determine signal/noise discrimination in pulsed-carrier systems," *Proc. IEEE* **51**(7), 1016–1027 (1963).
50. J. Y. Chen and I. S. Reed, "A detection algorithm for optical targets in clutter," *IEEE Trans. Aerosp. Electron. Syst.* **AES-23**(1), 46–59 (1987).
51. A. Plaza et al., "Foreword to the special issue on spectral unmixing of remotely sensed data," *IEEE Trans. Geosci. Remote Sens.* **49**(11), 4103–4109 (2011).
52. J. C. Mars and L. C. Rowan, "Regional mapping of phyllic- and argillic-altered rocks in the Zagros magmatic arc, Iran, using advanced spaceborne thermal emission and reflection radiometer (ASTER) data and logical operator algorithms," *Geosphere* **2**(3), 161–186 (2006).
53. J. C. Mars, "Hydrothermal alteration maps of the central and southern Basin and Range Province of the United States compiled from advanced spaceborne thermal emission and reflection radiometer (ASTER) data," U.S. Geological Survey Open File Report 2013–1139, p. 6, U.S. Geological Survey, Reston, Virginia (2013).

Fred A. Kruse received the PhD in geology from the Colorado School of Mines in 1987. He has been involved in remote sensing research and applications for over 30 years. He is currently a research professor at the Naval Postgraduate School, teaching spectral remote sensing and synthetic aperture radar. His research explores the distribution and character of earth-surface materials. He is also one of the scientists who originally developed the image analysis software ENVI.